Article   **Open Access**

The photometric system of the UCAS 70 cm Telescope

Yiming Mao[1,3] (iD), Liang Ge[1,2,3,7*] , Yongkang Sun[2,3] (iD), Jingxiao Luo[2,5,6], Xunhao Chen[2,3], Renhao Ye[2,4] (iD),

Lifu Zhang[2,5,6], Minglin Wang[2,3], E Xiang[2], Zhizhong Zhou[3], Hong Wu[2,3]

[1]*College of Science*, *Tibet University*, *Lhasa* 850000, *China*

[2]*School of Astronomy and Space Science*, *University of Chinese Academy of Sciences*, *Beijing* 100049, *China*

[3]*Key Laboratory of Optical Astronomy*, *National Astronomical Observatories*, *Chinese Academy of Sciences*, *Beijing* 100101, *China*

[4]*Shanghai Astronomical Observatory*, *Chinese Academy of Sciences*, *Shanghai* 200030, *China*

[5]*Yunnan Observatories*, *Chinese Academy of Sciences*, *Kunming* 650216, *China*

[6]*International Centre of Supernovae*, *Yunnan Key Laboratory*, *Kunming* 650216, *China*

[7]*Institute for Frontiers in Astronomy and Astrophysics*, *Beijing Normal University*, *Beijing* 100875, *China*

*Correspondence: geliang@bao.ac.cn

Abstract: This paper presents a comprehensive analysis of the photometric system of the University of Chinese Academy of Sciences 70 cm Telescope located at the Yan-qi Lake campus of the University of Chinese Academy of Sciences. We evaluated the linearity, bias stability, and dark current of the camera. Utilizing the Johnson-Cousins Blue-Visible-Red-Infrared filter system and an Andor DZ936 charge-coupled device camera, we conducted extensive observations of Landolt standard stars to determine the color terms, atmospheric extinction coefficients, photometric zero-points, and the sky background brightness. The results indicate that this telescope demonstrates excellent performance in photometric calibration and good system performance overall, meeting the requirements for limited scientific research and teaching purposes.

Keywords: Astronomical instrumentation; Astronomical detectors; Optical telescopes; Photometry; Astronomical techniques

1. INTRODUCTION

Located at the University of Chinese Academy of Sciences, Yan-qi Lake, Huairou, Beijing, the UCAS 70 cm Telescope (UCASST) is a Corrected Dall-Kirkham (CDK) telescope manufactured by Planewave Instruments[1]. The coordinates of the site are 40°24′34″N, 116°40′35″E at an altitude of 96 m above sea level. UCASST is managed by the School of Astronomy and Space Science at the University of Chinese Academy of Sciences and has been in operation for 2 years.

It is mainly used for student practice and research purposes. The main science activities conducted with UCASST in recent years concern cataclysmic variables (CVs), follow-up observations of supernovae (SNe), and studies on the occultation of Neptune's moon, Triton[1,2]. Major objectives performed by UCASST include the 50 Mpc Nearby Galaxies Survey, with the goal of long-term monitoring of nearby galaxies within 50 Mpc of Earth[3] to discover transient sources. Alongside the UCASST survey observations, we have also conducted follow-up observations of newly discovered transient sources.

UCASST has also been used for relatively simple tasks, which make good use of its observing time and are suitable for teaching. These tasks include investigating CVs. Each of these highly variable close binary systems consists of a white dwarf accreting material from a low-mass companion[4]. Their variability includes large or small outbursts, moderate periodic variations of hours, and fast variations on the order of seconds to kiloseconds[5]. Capturing their variability is crucial for

---

1. https://planewave.com/product/cdk700-0-7m-cdk-telescope-system/

understanding their basic properties, such as orbital periods and superhump periods, and for revealing their active and variable accretion processes. Although several time-domain sky surveys, such as All-Sky Automated Survey for Supernovae (ASAS-SN)[6] and Zwicky Transient Facility (ZTF)[7], have been ongoing, their sparse sampling intervals (typically spaced over several days) make dedicated monitoring an important objective. Consequently, we conducted a CV monitoring project using UCASST from 2022 to 2023, aiming to characterize some poorly known systems. The 70 cm aperture allows us to achieve a sufficient signal-to-noise ratio (SNR) in a single image to observe an object at magnitudes down to 15.5.

Despite accumulating a large amount of observational data, the comprehensive testing of UCASST is still incomplete. Here, we report observations of a large number of standard stars using a Blue-Visible-Red-Infrared (BVRI) filter system and an Andor DZ936 charge-coupled device (CCD) camera[2], providing systematic photometric zero-points, color index coefficients, and other parameters of UCASST, as well as measuring atmospheric extinction coefficients and on-site sky brightness. Additionally, we conducted a performance test of the camera to find out the linearity, bias stability, and dark current of the CCD.

The overall structure of the paper is as follows: basic parameters of the observation system and observations are introduced in Section 2, CCD test results are described in Section 3, photometric calibrations are presented in Section 4, the system performance of UCASST is presented in Section 5, the scientific results produced by UCASST are presented in Section 6, and the conclusions and discussions are presented in Section 7.

2. OBSERVATIONS

2.1. Observation System

UCASST is equipped with a CCD camera to fulfill observation requirements and will support spectrometry in the near future. The CDK optical system shows excellent optical quality. With a 4 557 mm focal length and F/6.5 focal ratio, the corrector enables a substantial 70 mm imaging circle. The UCASST filter system is equipped with seven filters, four of which are Johnson–Cousins BVRI filters[3]; the other three are Hα, [S II], and [O III] narrowband filters. Fig. 1 shows the transmission curves for UBVRI filters. Center wavelengths and half-width wavelengths are presented in Table 1.

In this work, all sources were observed using the Andor DZ936 CCD camera with the Johnson-Cousins BVRI filter system, the significant parameters of which are listed in Table 2 and Table 3. The combination of the telescope and the camera provides a resolution of 0.611″ pixel^{-1} with a 20.8′ × 20.8′ field of view (FoV).

2.2. Observations

We performed photometry on Landolt standard stars from September 30, 2023, to June 4, 2024. The observed
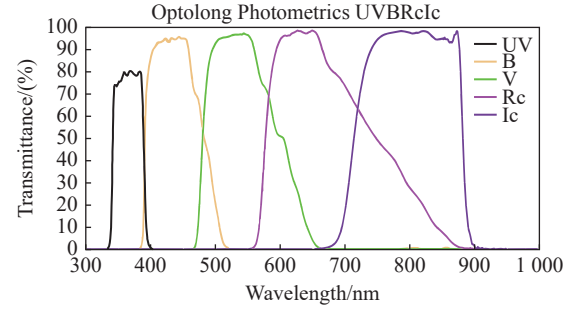

Fig. 1. Transmission curves for the Johnson–Cousins UBVRI filters manufactured by Optolong.

Table 1. Center wavelengths and half-width wavelengths of the Johnson–Cousins BVRI filters

Band Name	B	V	$R_{Cousins}$	$I_{Cousins}$
λc/nm	38.4	40.0	668.1	814.2
Δλ/nm	0	40	180	160

Table 2. Parameters of the Andor DZ936 CCD camera

Features	Specifications
Pixel number	$2\,048 \times 2\,048$
Pixel size	13.5 μm × 13.5 μm
Imaging area	27.6 mm × 27.6 mm
AD conversion	16 Bit
Scan rates	50 kHz, 1 MHz, 3 MHz, 5 MHz
Read noise @ 1MHz	6.4 e$^-$
Software-selectable gains	1×, 2×, 4×
Gain @ 4x mode	1.0 e$^-$/ADU
Dark current	0.001 e^{-1} pix^{-1} s^{-1}@ −70°C
Nonlinearity	<1%

Table 3. Main parameters of the Planewave CDK700 observatory system

Features	Specifications
Optical design	Corrected Dall-Kirkham
Focal length	4 557 mm
Aperture	700 mm
Focal ratio	F/6.5
Image circle	70 mm
Image scale	22 μm/(″)
Focus port	Two Nasmyth focus ports
Mount type	Alt/Az
Motors	Direct drive motors with encoders
Maximum speed	10°/s

stars[8] are listed in Table 4. and the observation logs are given in Table 5. Here we should note that we generated Table 4. by cross-matching the observed standard stars with the Landolt catalog and extracting the matched items

---

Table 4. Landolt's standard stars used for photometric calibration

Star	α(J2000)	δ(J2000)	V_{mag}	$B_{\mathrm{mag}}-V_{\mathrm{mag}}$	$V_{\mathrm{mag}}-R_{\mathrm{mag}}$	$R_{\mathrm{mag}}-I_{\mathrm{mag}}$
SA 92250	00 54 37	+00 38 56	13.178	0.814	0.446	0.394
SA 92253	00 54 52	+00 40 20	14.085	1.131	0.719	0.616
SA 92347	00 55 26	+00 50 49	15.752	0.543	0.339	0.318
SA 92348	00 55 30	+00 44 34	12.109	0.598	0.345	0.341
SA 93317	01 54 38	+00 43 00	11.546	0.488	0.293	0.298
SA 94171	02 53 38	+00 17 19	12.659	0.81	0.480	0.483
SA 94242	02 57 21	+00 18 38	11.728	0.301	0.178	0.184
SA 94296	02 55 20	+00 28 14	12.255	0.750	0.415	0.387
SA 94394	02 56 14	+00 35 10	12.273	0.545	0.344	0.330
SA 94401	02 56 31	+00 40 05	14.293	0.63	0.389	0.369
SA 94702	02 58 13	+01 10 53	11.594	1.418	0.756	0.673
SA 9515	03 52 40	−00 05 22	11.302	0.712	0.424	0.385
SA 9566	03 55 07	−00 09 31	12.892	0.715	0.426	0.438
SA 104461	12 43 07	−00 32 21	9.705	0.476	0.289	0.290
SA 113167	21 42 41	+00 16 08	14.841	−0.034	0.351	0.376
SA 114548	22 41 37	+00 59 07	11.601	1.362	0.738	0.651
PG0231+051	02 33 41	+05 18 40	16.105	−0.329	−0.16	−0.371
PG2213−006	22 16 28	−00 21 15	14.124	−0.217	−0.092	−0.110

Table 5. Observation log table of stars from the Landolt catalog

Observation Date (yyyy/mm/dd)	Target	Band	Exposure time/s	Frames per band
	SA 113167	B, V, R, I	10	54
	SA 114548	B, V, R, I	10	10
2023/11/11	PG0231+051	B, V, R, I	10	28
	PG2213−006	B, V, R, I	10	45
2023/11/12	SA 92253	B, V, R, I	10	12
	PG0231+051	B, V, R, I	10	23
2023/11/16	PG0231+051	B, V, R, I	30	30
2023/11/17	SA 93317	B, V, R, I	30	18
	PG0231+051	B, V, R, I	30	12
2023/11/18	SA 92348	B, V, R, I	30	30
	SA 93317	B, V, R, I	30	30
	SA 94171	B, V, R, I	30	29
2023/11/19	SA 94296	B, V, R, I	30	29
	SA 94394	B, V, R, I	30	16
2023/11/23	SA 94242	B, V, R, I	30	24
	SA 94401	B, V, R, I	30	29
2023/11/24	SA 9515	B, V, R, I	30	33
	SA 94401	B, V, R, I	30	30
2023/11/25	SA 95301	B, V, R, I	10	21
2023/12/01	SA 94401	B, V, R, I	30	30
	SA 94702	B, V, R, I	30	13
2023/12/02	SA 94242	B, V, R, I	30	30
	SA 9515	B, V, R, I	30	54
	SA 92250	B, V, R, I	30	20
2023/12/03	SA 94242	B, V, R, I	30	27
	SA 9515	B, V, R, I	30	23
2023/12/04	SA 92347	B, V, R, I	30	68
	SA 9566	B, V, R, I	30	32
2024/05/30	SA 104461	B, V, R, I	10	18

from the catalog. The complete Landolt catalog can be obtained through the Vizier website[4]. Table 5 includes the names of the observed standard stars, observation bands, exposure times, and the number of images taken for each band. We switched the filter after each exposure to ensure that the observation conditions for each band were as similar as possible.

Several cloudless, moonless photometric nights with good air quality were chosen during the target time period to perform accurate flux calibrations for UCASST using observed standard star data. Additionally, we determined the atmospheric extinction coefficient of the site by observing some star fields. For CCD testing, bias images were taken from June 6–8, 2024, for more than 30 hours, to test the bias stability. Tests for gain and readout noise used conventional observational data, and dome flat images were taken on June 16, 2024, to test the linearity.

3. CCD CALIBRATIONS

3.1. Bias

CCD bias refers to the baseline or offset voltage level present in each pixel of a CCD sensor during image capture. Bias is dependent on the characteristics of the CCD is being used, and by taking bias images with a 0-second exposure (i.e., direct readout with no exposure). By subtracting this biased image during image processing, we can correct the errors caused by the CCD bias. Bias stability has a significant impact on photometric accuracy.

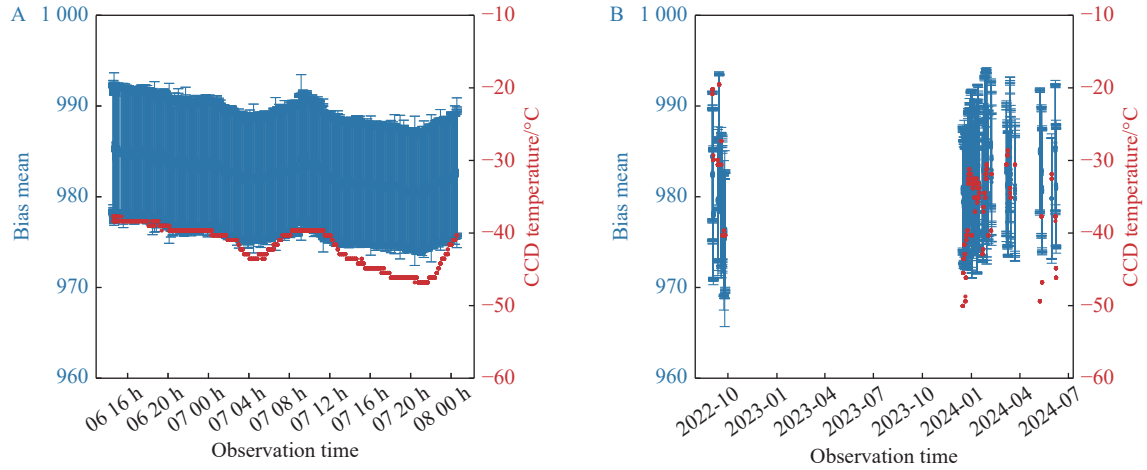To test the bias stability, bias images were taken over 30 hours, with the results shown in Fig. 2A. We took 10

---

4. https://vizier.cds.unistra.fr/viz-bin/VizieR-3?-source=II/183A

Fig. 2. Stability test results on the bias of the Andor DZ936 CCD camera. The bias stability test results over 30 consecutive hours are shown in (A), and the long-term stability during over 20 months are shown in (B). The mean values and standard errors of these bias groups are shown as blue points with error bars, while the CCD temperature is shown with red dots.

individual bias images with an exposure time of 0 s as a "bias group" for each observation, with a time interval of 10 minutes between each bias group.

For the long timespan bias test, bias data taken between September 2022 and June 2024 are shown in Fig. 2B. Similarly to the previous method, the bias group here was composed of bias images all recorded on the same day, providing a single data point. On the basis of these data, we concluded that the bias was stable and correlated with the temperature of the CCD during the observations. For longer timespans, the mean value of the bias did not change by much. Therefore, a single master bias can be used over the whole night, without involving time-variable corrections. Here we should note that the CCD temperature was not constant because of instabilities in the power supply at the observation site. At constant temperature, it is likely that the change in the bias will decrease.

3.2. Gain and Readout Noise

The gain and the read noise of the Andor DZ936 camera were tested. CCD gain is a parameter that describes the conversion factor between the number of electrons recorded in each pixel and the corresponding analog-to-digital units (ADU) that the camera outputs.

It is typically measured in electrons per ADU (e$^-$/ADU). Knowing this value helps to evaluate the performance of a CCD. CCD readout noise is the electronic noise introduced during the process of reading out the charge from each pixel and converting it to a digital signal, and is measured in electrons (e$^-$).

To give the gain and readout noise, two bias frames and two flat frames are needed[9]. The basic formulas for calculating the gain (G) and readout noise (R_N) are:

$$G = \frac{\overline{F_1} - \overline{B_1} + \overline{F_2} - \overline{B_2}}{\sigma^2_{F_1-F_2} - \sigma^2_{B_1-B_2}} \tag{1}$$

and

$$R_\text{N} = \frac{G\left(\sigma_{B_1-B_2}\right)}{\sqrt{2}}, \tag{2}$$

where F_1 and F_2 are the mean values of two independent flat images, while B_1 and B_2 are the mean values of two independent bias images. $\sigma_{F_1-F_2}$ and $\sigma_{B_1-B_2}$ are the standard deviation of the difference image of two independent flat images and the standard deviation of the difference image of two independent bias images, respectively.

A few days of twilight flat fields with different exposure times were chosen to test the gain and readout noise. We used the 4x mode of the Andor DZ936 camera, with a readout speed of 1 MHz. Detailed specifications given by the manufacturer can be found in Table 3, and our test results are shown in Table 6.

We found that the readout noise and the gain were stable over a long period of operation. The values of readout noise were comparatively lower than the corresponding values given by the manufacturer, and the gain values were similar to the corresponding value given by the manufacturer.

Table 6. Test results for gain and readout noise

Test date	Readout mode	Readout noise/ (e$^-$)	Gain/ (e$^-$/ADU)	Average readout noise/(e$^-$)	Average gain /(e$^-$/ADU)
2024/02/01	4x @ 1 MHz	4.098 ± 0.017	0.985 ± 0.004		
2024/03/09	4x @ 1 MHz	4.354 ± 0.018	1.043 ± 0.004		
2024/03/13	4x @ 1 MHz	4.344 ± 0.018	1.003 ± 0.004	4.322 ± 0.018	1.024 ± 0.004
2024/03/22	4x @ 1 MHz	4.444 ± 0.019	1.044 ± 0.004		
2024/05/11	4x @ 1 MHz	4.534 ± 0.019	1.039 ± 0.004		
2024/05/12	4x @ 1 MHz	4.157 ± 0.017	1.029 ± 0.004		

3.3. Linearity

To test the linearity of the CCD camera, a stable in-dome light source was used to measure the ADU counts as a function of exposure time. We took these linearity test data in 4x mode at night on June 16, 2024, with the exposure times ranging from 2.0 s to 1800 s. Linearity test results are shown in Fig. 3. When the ADU count value was below 10 000, the Andor DZ936 camera exhibited excellent linearity with a correlation coefficient of 0.999 996. Over the entire range of the ADU count value up to 60 000, the camera still kept perfect linearity, with a correlation coefficient of 0.999 974.
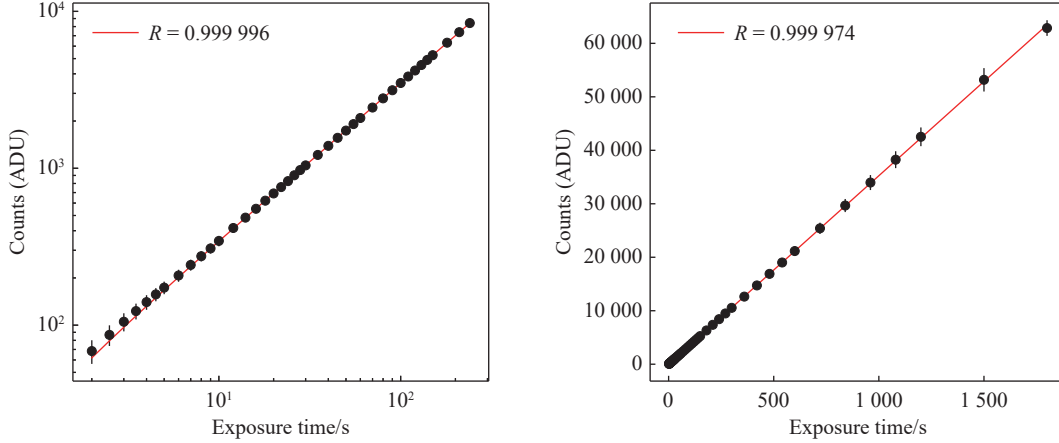

Fig. 3. Linearity test results of the Andor DZ936 camera. The correlation coefficients are 0.999 996 and 0.999 974 for ADU counts up to 10 000 and counts over the entire interval, respectively.

3.4. Dark Current

Dark current is usually generated by the accumulation of electrons in the potential well of each pixel, and is expressed as the number of thermal electrons generated per second per pixel (e^- pix^{-1} s^{-1}). These signals, generated by thermal electrons, are indiscernible from light photons but can be ignored if the generation rate is low enough. Dark frames in this work were obtained on September 19 and 20, 2022, with integration times of 60 s, 120 s, 180 s, 300 s, and 600 s. We measured that the mean generation rate of the Andor DZ936 camera at –40°C was 0.074 e^- pix^{-1} s^{-1}. This dark current is relatively low, so dark correction can be neglected for short exposure observations.

4. PHOTOMETRIC CALIBRATIONS

To convert between the instrumental magnitude obtained by UCASST and the standard magnitude found in Landolt or other BVRI catalogs, precise photometric calibration is needed. Transform equations of a photometric calibration can be expressed as:

$$b = B_{mag} + Z_B + k'_B X + C_B(B_{mag} - V_{mag}), \quad (3)$$

$$v = V_{mag} + Z_V + k'_V X + C_V(V_{mag} - R_{mag}), \quad (4)$$

$$r = R_{mag} + Z_R + k'_R X + C_R(V_{mag} - R_{mag}), \quad (5)$$

and

$$i = I_{mag} + Z_I + k'_I X + C_I(R_{mag} - I_{mag}), \quad (6)$$

where b, v, r, and i are the instrumental magnitudes normalized to the exposure time of 1s, B_{mag}, V_{mag}, R_{mag}, and I_{mag} are the standard magnitudes obtained by Landolt[8], Z_B, Z_V, Z_R, and Z_I are the zero-point magnitudes of the transformation, k'_B, k'_V, k'_R, and k'_I are the first-order atmospheric extinction coefficients, X is the airmass, C_B, C_V, C_R, and C_I are the color terms, and $B_{mag} - V_{mag}$, $V_{mag} - R_{mag}$, and $R_{mag} - I_{mag}$ are the color indices of the standard stars.

Here, photometry was performed using the sep[5] package, based on Python. The main photometric processes include bias combination, flat combination, CCD processing, World Coordinate System solving, background subtraction, and aperture photometry.

4.1. Color Terms

By observing bright Landolt standard star fields or open clusters, we can determine the color terms for the transformations[10]. When calculating these two parameters, different stars in the same FoV were used, so their airmasses can be considered to be the same. This allows Equations (3)–(6) to be rewritten as:

$$b = B_{mag} + Z_B + C_B(B_{mag} - V_{mag}) + constant, \quad (7)$$

$$v = V_{mag} + Z_V + C_V(V_{mag} - R_{mag}) + constant, \quad (8)$$

$$r = R_{mag} + Z_R + C_R(V_{mag} - R_{mag}) + constant, \quad (9)$$

---

5. https://sep.readthedocs.org/

and

$$i = I_{\text{mag}} + Z_I + C_I(R_{\text{mag}} - I_{\text{mag}}) + \text{constant}. \qquad (10)$$

From these equations, we can easily include different stars in the same FoV, with varying colors, to determine the color terms. Measurement results using differ-

ent star fields, taken on different days, are presented in Table 7. Color terms were calculated from single or multiple star fields using the linear fitting method from the curvefit function in the scipy Python package. For the multiple star fields, weighted averages were performed to obtain a relatively accurate result. The overall result is the average value of the results obtained from every single date.

Table 7. Measured color terms

Test date	Center field star	$C_B \pm \sigma_{C_B}$	$C_V \pm \sigma_{C_V}$	$C_R \pm \sigma_{C_R}$	$C_I \pm \sigma_{C_I}$
2023/11/11	SA 113167	0.239 ± 0.012	-0.151 ± 0.010	-0.071 ± 0.009	-0.334 ± 0.012
	PG0231+051	−	0.075 ± 0.029	0.082 ± 0.033	−
	PG2213−006	0.202 ± 0.006	-0.045 ± 0.007	0.042 ± 0.008	-0.197 ± 0.012
	Weighted Average	0.209 ± 0.005	-0.071 ± 0.005	-0.004 ± 0.006	-0.265 ± 0.008
2023/11/12	SA 92253	0.239 ± 0.005	0.117 ± 0.003	0.183 ± 0.002	0.015 ± 0.003
	SA 92330	0.257 ± 0.015	-0.007 ± 0.007	0.114 ± 0.003	-0.054 ± 0.004
	PG0231+051	0.211 ± 0.015	0.033 ± 0.007	0.108 ± 0.004	−
	Weighted Average	0.238 ± 0.005	0.083 ± 0.003	0.148 ± 0.002	-0.017 ± 0.002
2023/11/16	PG0231+051	0.453 ± 0.008	-0.009 ± 0.006	0.107 ± 0.003	-0.100 ± 0.006
2023/11/17	PG0231+051	0.132 ± 0.018	0.008 ± 0.012	0.116 ± 0.007	-0.054 ± 0.007
2023/11/25	SA 95102	−	−	0.074 ± 0.006	-0.256 ± 0.011
	SA 95301	−	-0.006 ± 0.006	0.058 ± 0.004	-0.065 ± 0.006
	Weighted Average	−	-0.006 ± 0.006	0.064 ± 0.003	-0.109 ± 0.005
2023/12/02	SA 9515	0.151 ± 0.001	-0.046 ± 0.001	0.025 ± 0.001	-0.161 ± 0.001
2023/12/03	SA 9515	0.187 ± 0.002	-0.004 ± 0.002	0.023 ± 0.002	-0.167 ± 0.002
	SA 92250	0.119 ± 0.011	-0.022 ± 0.006	0.069 ± 0.003	-0.106 ± 0.002
	Weighted Average	0.184 ± 0.002	-0.006 ± 0.002	0.033 ± 0.001	-0.142 ± 0.002
2024/05/30	SA 104461	0.230 ± 0.020	0.071 ± 0.006	0.083 ± 0.003	-0.131 ± 0.005
	Overall Average	0.228 ± 0.008	0.003 ± 0.005	0.072 ± 0.003	-0.122 ± 0.005

4.2. Atmospheric Extinction Coefficient

The atmospheric extinction coefficient is an important parameter for measuring atmospheric conditions at an observation site, and by measuring it with different filters, we are able to obtain the atmospheric extinction coefficients of different bands[11]. Because we are only concerned with the variation of one individual standard star with one airmass, the color term is held constant.

Here, Equations (3)–(6) can be rewritten as:

$$b = B_{\text{mag}} + Z_B + k'_B X + \text{constant}, \qquad (11)$$

$$v = V_{\text{mag}} + Z_V + k'_V X + \text{constant}, \qquad (12)$$

$$r = R_{\text{mag}} + Z_R + k'_R X + \text{constant}, \qquad (13)$$

and

$$i = I_{\text{mag}} + Z_I + k'_I X + \text{constant}, \qquad (14)$$

where k'_B, k'_V, k'_R, and k'_I are the first-order atmospheric extinction coefficients. We assume that the atmospheric extinction coefficient k' does not change with time, so that it can be obtained easily using linear fitting. Fig. 4

gives an example of fitting the atmospheric extinction coefficient. The photometric data of SA 114 514 was observed on November 11, 2023, which was a clear and moonless photometric night. Several standard stars in the field were used to give the values of k' in different bands. Weighted averages were performed for different stars in the same band to give a relatively precise value of the k'. Final results are presented in Table 8.

4.3. Photometric Zero-points

After finding the values of color terms and atmospheric extinction coefficients, photometric zero-points of each band can be easily calculated using Equations (3)–(6). We used the mean value of the photometric zero-points of each star as the zero-point for a single image, and used the same method on each image as the zero-point for an entire photometric night.

In Table 9, we show photometric zero-points from different nights. The photometric zero-points show the effect of the observation environment and the instrument. For the photometric nights during November and December of 2023, the photometric zero-points were relatively stable. For the photometric observations on May 30, 2024, the zero-point was approximately 1.7 lower in each band, which indicated a change in the observing environment. We will further discuss this in Section 7.
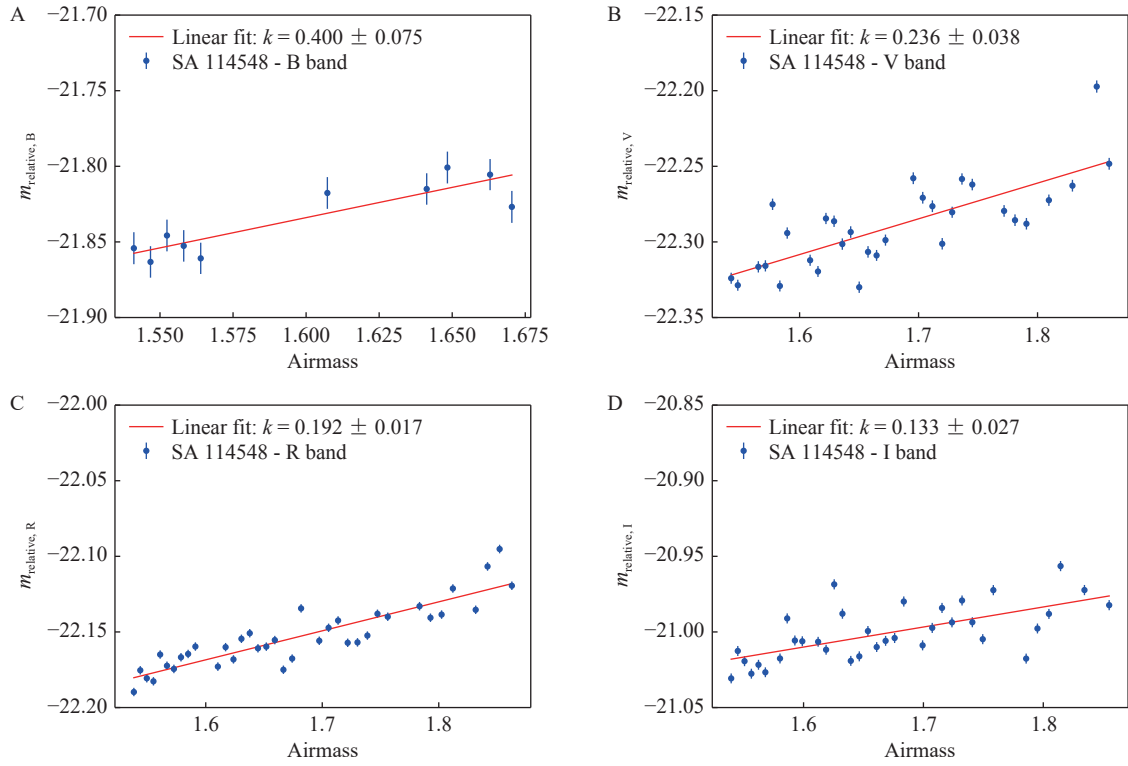
Fig. 4. Images of atmospheric extinction coefficients obtained using Landolt standard stars in different bands. The *x*-axis shows airmass and the *y*-axis shows the difference between instrumental magnitude and standard magnitude presented in the Landolt catalog. The BVRI bands are plotted in (A), (B), (C), and (D).

Table 8. Measured atmospheric extinction coefficients

Test date	$k'_B \pm \sigma_{k'_B}$	$k'_V \pm \sigma_{k'_V}$	$k'_R \pm \sigma_{k'_R}$	$k'_I \pm \sigma_{k'_I}$
2023/11/11	0.322 ± 0.031	0.165 ± 0.018	0.156 ± 0.014	0.136 ± 0.018
2023/11/12	0.261 ± 0.022	0.177 ± 0.015	0.171 ± 0.011	0.079 ± 0.013
2023/11/16	0.320 ± 0.038	0.239 ± 0.016	0.145 ± 0.012	0.083 ± 0.021
2023/11/19	0.437 ± 0.051	0.288 ± 0.029	0.223 ± 0.021	0.168 ± 0.017
2023/11/23	0.314 ± 0.019	0.256 ± 0.019	0.181 ± 0.013	0.120 ± 0.018
2023/12/02	0.359 ± 0.015	0.286 ± 0.008	0.221 ± 0.008	0.151 ± 0.006
2024/05/30	−	0.114 ± 0.007	0.046 ± 0.006	0.012 ± 0.006
Overall average	0.336 ± 0.029	0.218 ± 0.016	0.163 ± 0.012	0.107 ± 0.014
Mu et al.[12]	0.335 ± 0.022	0.193 ± 0.018	0.090 ± 0.013	0.070 ± 0.017

Table 9. Measured photometric zero-points

Test date	$Z_B \pm \sigma_{Z_B}$	$Z_V \pm \sigma_{Z_V}$	$Z_R \pm \sigma_{Z_R}$	$Z_I \pm \sigma_{Z_I}$
2023/11/11	−22.421 ± 0.161	−22.637 ± 0.090	−22.472 ± 0.079	−21.201 ± 0.083
2023/11/12	−22.387 ± 0.140	−22.632 ± 0.044	−22.433 ± 0.048	−21.108 ± 0.069
2023/11/16	−22.360 ± 0.301	−22.657 ± 0.011	−22.453 ± 0.066	−21.113 ± 0.057
2023/11/17	−22.380 ± 0.188	−22.636 ± 0.039	−22.436 ± 0.051	−21.233 ± 0.203
2023/11/18	−22.157 ± 0.148	−22.510 ± 0.066	−22.302 ± 0.045	−21.037 ± 0.052
2023/11/19	−22.174 ± 0.049	−22.479 ± 0.033	−22.249 ± 0.027	−21.017 ± 0.007
2023/11/23	−22.383 ± 0.156	−22.612 ± 0.048	−22.405 ± 0.023	−21.143 ± 0.047
2023/12/02	−22.361 ± 0.163	−22.552 ± 0.075	−22.367 ± 0.040	−21.065 ± 0.052
2024/05/30	−21.683 ± 0.146	−21.755 ± 0.053	−21.622 ± 0.038	−20.315 ± 0.074

4.4. Calibration Results

We used the data from November 18, 2023, for the photometric transformations and plotting, and results are shown in Fig. 5.

The standard deviations of the BVRI bands are 0.105, 0.040, 0.033, and 0.036, respectively. This means that we can make good transformations from instrumental magnitude to the standard Johnson–Cousins system.
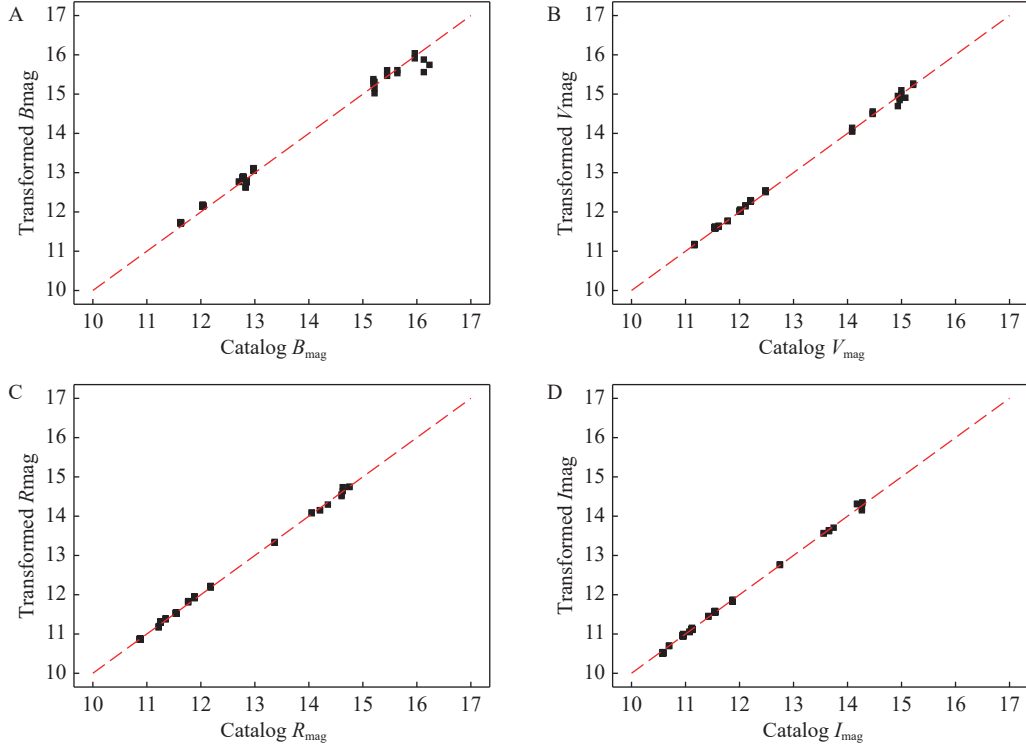
Fig. 5. Transformation fitting results for the BVRI bands. The data used for plotting was observed on November 18, 2023. The dotted red line shows the ideal transformation result, and the fitting slope from the data point is very close to 1.

This can be performed using the equations:

$$b = (-22.157 \pm 0.148) + (0.336 \pm 0.029)X +$$
$$(0.228 \pm 0.008)(B_{\mathrm{mag}} - V_{\mathrm{mag}}) + B_{\mathrm{mag}}, \ \sigma = 0.105, \quad (15)$$

$$v = (-22.510 \pm 0.066) + (0.218 \pm 0.016)X +$$
$$(0.003 \pm 0.005)(V_{\mathrm{mag}} - R_{\mathrm{mag}}) + V_{\mathrm{mag}}, \ \sigma = 0.040, \quad (16)$$

$$r = (-22.302 \pm 0.045) + (0.163 \pm 0.012)X +$$
$$(0.072 \pm 0.003)(V_{\mathrm{mag}} - R_{\mathrm{mag}}) + R_{\mathrm{mag}}, \ \sigma = 0.033, \quad (17)$$

and

$$i = (-21.037 \pm 0.052) + (0.107 \pm 0.014)X +$$
$$(-0.122 \pm 0.005)(R_{\mathrm{mag}} - I_{\mathrm{mag}}) + I_{\mathrm{mag}}, \ \sigma = 0.036. \quad (18)$$

5. SYSTEM PERFORMANCE

5.1. System Throughput

System throughput gives the overall efficiency, including the efficiency of optical components, transmission of the filters, quantum efficiency of the detector, and the transmission of the atmosphere[13]. The system throughput can be calculated as:

$$E_\lambda = F_\lambda 10^{-0.4\ m_\lambda} \pi \left(\frac{D}{2}\right)^2 \Delta\lambda, \quad (19)$$

which finds the energy intake per second from a star of

magnitude m_λ in a circle of diameter D outside the Earth's atmosphere. Here, F_λ represents the flux of a 0-magnitude star at wavelength λ, and $\Delta\lambda$ represents the half-width of the transmission wavelength of the filter.

After finding E_λ, we can further calculate the incoming photons (N_{calc}) as:

$$N_{\mathrm{calc}} = \frac{E_\lambda}{h\nu} = \frac{E_\lambda \lambda}{hc}, \quad (20)$$

where h is the Planck constant and c is the speed of light. We can also calculate the extinction-corrected count rate of the CCD (N_{obs}) as:

$$N_{\mathrm{obs}} = \frac{C_{\mathrm{raw}}}{T_{\mathrm{exp}}} 10^{-0.4kX} G, \quad (21)$$

where C_{raw} is the integrated count of the star, T_{exp} is the exposure time, k is the first-order atmospheric extinction coefficient, X is the airmass, and G is the gain of the CCD. The total throughput E is defined as:

$$E = \frac{N_{\mathrm{obs}}}{N_{\mathrm{calc}}}. \quad (22)$$

Our calculation results are given in Table 10. Here we find a similar situation to the results of the photometric zero-points in Section 4.3, with the system throughput reaching its lowest on May 30, 2024.

5.2. Sky Background Brightness

Sky background brightness is a significant reference for performing observations. To estimate the sky bright-

ness, we used the background functions in the photoutils Python package to extract and measure the flux of the sky background, which was transformed and normalized using Equations (3)–(6). The color terms and atmospheric extinction coefficients use the overall average values given in Table 7 and Table 8. Zero-points for each day can be found in Table 9.

The sky background brightnesses, measured on different days, are shown in Table 11, expressed in units of mag/arcsec^2. The illumination of the Moon is shown in the last column, and the values in parentheses indicate the angle of the target from the Moon during the observation.

On moonless photometric nights during November and December of 2023, the mean sky background brightness values of the BVRI bands were ~19.87 in the B band, ~19.02 in the V band, ~19.16 in the R band, and ~19.19 in the I band. During the moonless photometric night on May 30, 2024, the sky background brightness increased substantially, and significantly correlates with a drop in zero-point magnitude and system throughput. Comparisons with observations taken at the Yan-qi Lake Obser-

Table 10. System throughput of different bands

Date	System throughput/(%)			
	B	V	R	I
2023/11/11	11.26	11.89	7.15	2.46
2023/11/12	10.19	12.16	6.98	2.43
2023/11/16	11.57	13.02	7.38	2.58
2023/11/17	12.06	13.34	7.49	2.63
2023/11/18	8.81	11.33	6.62	2.44
2023/11/19	9.00	10.77	6.15	2.28
2023/11/23	9.70	12.26	6.95	2.57
2023/12/02	8.11	10.33	5.99	2.27
2024/05/30	4.82	5.57	3.29	1.12

vatory and other professional observatories are shown in Table 12. We find that the night sky brightness at Yan-qi Lake is much higher than most other professional observatories, and compared with that in 2023, the night sky brightness in 2024 has significantly increased. We have subsequently communicated with the relevant departments of the Yan-qi Lake campus and made efforts to control light pollution near the observatory.

Table 11. Mean sky background brightnesses in various photometric bands

Date	Mean sky background brightness/(mag/arcsec^2)				Moon illumination/(%)
	B	V	R	I	
2023/11/11	19.53 ± 0.24	18.67 ± 0.20	18.90 ± 0.18	19.31 ± 0.22	3.5 (Below horizon)
2023/11/12	19.97 ± 0.16	19.07 ± 0.16	19.16 ± 0.13	19.03 ± 0.14	1.0 (Below horizon)
2023/11/16	20.21 ± 0.03	19.40 ± 0.04	19.48 ± 0.04	19.09 ± 0.09	10.7 (Below horizon)
2023/11/17	19.75 ± 0.35	18.92 ± 0.26	19.11 ± 0.19	19.34 ± 0.09	18.5 (Below horizon)
2023/11/18	19.02 ± 0.11	18.13 ± 0.15	18.25 ± 0.16	18.90 ± 0.12	27.9 (58°)
2023/11/19	19.00 ± 0.22	18.14 ± 0.15	18.26 ± 0.14	18.78 ± 0.16	38.7 (33°)
2023/11/23	18.65 ± 0.06	17.90 ± 0.04	17.89 ± 0.07	17.74 ± 0.21	82.1 (34°)
2023/12/02	19.26 ± 0.16	18.36 ± 0.15	18.57 ± 0.13	19.06 ± 0.05	74.5 (78°)
2024/05/30	19.10 ± 0.04	18.06 ± 0.18	18.31 ± 0.18	18.38 ± 0.08	50.0 (Below horizon)

5.3. Limiting Magnitude and Photometric Precision

The SNR of an observed object[9] can be calculated as:

$$R_{SN} = \frac{N_{star}}{\sqrt{N_{star} + n_{pix}\left(N_S + N_D + N_R^2\right)}}, \quad (23)$$

where N_{star} is the total number of photons received from the source, N_S, N_D, and N_R are the total number of photons given by the sky background, the dark current per pixel, and the CCD readout noise (in Section 3.2), respectively. n_{pix} is the whole pixel area used for the SNR calculation. Table 13 shows the limiting magnitudes of the different moonless photometric nights with corresponding exposure time when $R_{SN} = 10$.

Table 12. Sky background brightnesses at different observatories

Observatory	Sky background brightness/(mag/arcsec^2)				Reference
	B	V	R	I	
Xinglong	21.70	21.20	20.50	19.10	Shi et al.[14]
	20.90	20.00	19.30	18.10	Huang et al. [10]
Lulin	22.00	21.3	21.00	19.50	Kinoshita et al. [13]
Weihai	20.17	18.90	18.95	19.11	Hu et al.[15]
La Palma	22.70	21.90	21.00	20.00	Benn & Ellison[16]
Paranal	22.60	21.60	20.90	19.70	Patat[17]
Yan-qi Lake (2023)	19.87	19.02	19.16	19.19	this work
Yan-qi Lake (2024)	19.10	18.06	18.31	18.38	this work

Table 13. Limiting magnitudes of BVRI bands measured on moonless photometric nights

Date	Limiting magnitude/mag				Exposure time/s
	B	V	R	I	
2023/11/11	15.54	15.57	15.60	15.19	10
2023/11/12	15.50	15.78	15.70	15.00	10
2024/05/30	14.94	14.70	15.16	14.50	10
2023/11/16	16.73	16.80	16.62	16.04	30
2023/11/17	16.31	16.23	16.24	16.20	30

The limiting magnitudes for $R_{SN} = 10$, with an exposure time of 10 s in November 2023, are 15.5 in the B band, 15.7 in the V band, 15.6 in the R band, and 15.1 in the I band; they decrease to 14.9 in the B band, 14.7 in the V band, 15.2 in the R band, and 14.5 in the I band during May of 2024.

The limiting magnitudes at $R_{SN} = 10$, with a 30 s exposure during November 2023, are 16.5 in the B band, 16.5 in the V band, 16.4 in the R band and 16.1 in the I band.

The errors of Landolt standard stars observed on moonless photometric nights are shown in Fig. 6. The photometric precision of a 30 s exposure is ≤0.01 mag for stars brighter than 13.6 in the B and V bands, 13.5 in the R band, and 13.0 in the I band. For an exposure time of 10 s, the corresponding values are 13.0 in the B, V, and R bands, and 12.4 in the I band.
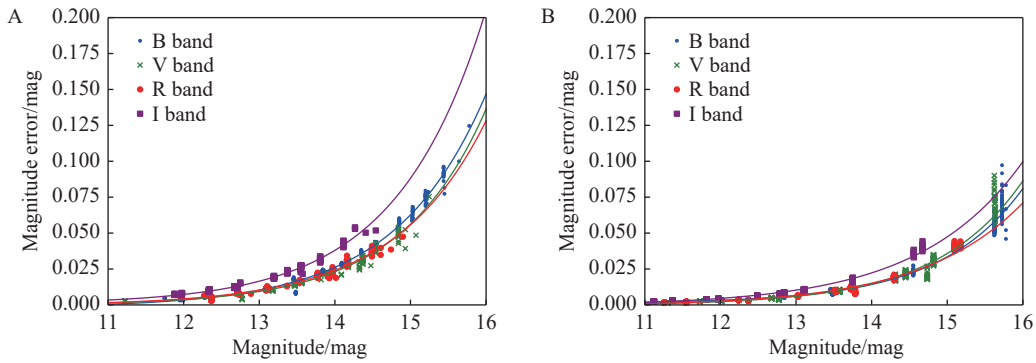

Fig. 6. Magnitudes plotted against magnitude errors for moonless photometric nights. (A) the magnitudes against magnitude errors for a 10 s exposure time. (B) the same for a 30 s exposure time.

6.　RESULTS

Because UCASST has a relatively low limiting magnitude, it is well-suited to observing bright sources such as supernovae and bright variables. Taking this into consideration, we organized two different observing tasks on UCASST, including the Nearby Galaxies Survey and the Cataclysmic Variables Monitoring Program.

For the Nearby Galaxies Survey, UCASST is capable of performing both survey and follow-up observations of transient targets because of its medium-sized FoV. The observed targets are shown in Table 14, including nearby galaxies and supernovae.

We acquired and compiled these notable supernovae from the Transient Naming Server[6] (TNS), and performed long-term observations. For the galaxies presented, we only concentrated on the relatively near and bright galaxies because of the low detection efficiency of UCASST.

For the Cataclysmic Variables Monitoring Program, we selected two CVs observed by the Large Sky Area Multi-Object Fiber Spectroscopic Telescope (LAMOST) from Hou et al.[18] and Sun et al.[19] and a W Ursae Majoris-type eclipsing variable (EW-type) as observing targets. Specifically, we observed the bright ($g_{mag} = 13.3$) nova-like star LAMOST J0925 (first reported by Hou et al.[18]) over seven nights using Johnson V or R filters with a 20 s exposure time.

We performed differential photometry using circular apertures, and the resulting light curves clearly show significant rapid variations on a timescale of several minutes (see Fig. 7), which are likely due to accretion-induced flickering or quasi-periodic oscillations. The magnitude error of the target and the magnitude standard deviation of a nearby check star (which is approximately 0.06 mag fainter than the target) are both less than 0.01 mag. We also acquired light curves over 10 nights for the CV candidate LAMOST J0148 ($g_{mag} = 15.4$, reported in Sun et al.[19]). The R band light curves give good results, compared with Transiting Exoplanet Survey Satellite (TESS) observations (see Fig. 8—note that the TESS fluxes are contaminated by a nearby source). The original 20-second cadence TESS light curve is binned to a 180-second cadence to match the 180-second exposure time of the UCASST observation. With a narrower filter bandwidth than that of TESS, UCASST achieves a higher SNR, demonstrating the ability of the telescope to observe relatively faint sources. Interestingly, there is an EW-type eclipsing variable star ATO J027+36 in the same FoV. The averaged V band magnitude of this variable is 15.49. In Fig. 9 we present the V and R band light curves of the EW-type variable, which are folded using a period of

_____

Table 14. Targets observed by the Nearby Galaxies Survey

| Name	R.A.	Dec.	Object Type	Total observations (Days)
SN 2023bvj	09 : 50 : 56	+33 : 33 : 11	SN	20
SN 2023ixf	14 : 03 : 39	+54 : 18 : 42	SN	76
SN 2023wuk	22 : 19 : 30	+29 : 23 : 18	SN	7
SN 2023zqy	11 : 15 : 22	+31 : 31 : 25	SN	13
SN 2024gy	12 : 15 : 51	+13 : 06 : 56	SN	21
SN 2024jz	15 : 33 : 05	−01 : 37 : 30	SN	19
SN 2024ka	12 : 04 : 10	+01 : 49 : 34	SN	20
SN 2024ws	08 : 28 : 40	+73 : 44 : 53	SN	21
SN 2024any	03 : 08 : 57	−02 : 57 : 19	SN	10
SN 2024apt	10 : 25 : 37	−02 : 12 : 40	SN	12
SN 2024bch	10 : 21 : 48	+56 : 55 : 49	SN	11
M 61	12 : 21 : 55	+04 : 28 : 26	G	41
M 77	02 : 42 : 41	−00 : 00 : 48	G	34
M 81	09 : 55 : 33	+69 : 03 : 55	G	45
M 109	11 : 57 : 36	+53 : 22 : 28	G	37
NGC 2841	09 : 22 : 03	+50 : 58 : 35	G	33
NGC 6946	20 : 34 : 52	+60 : 09 : 13	G	28
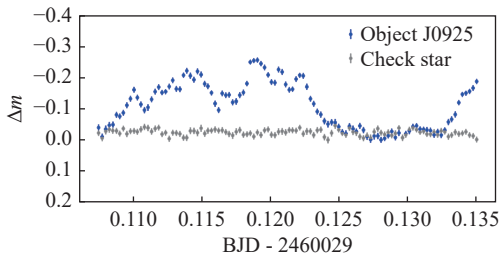
Fig. 7. The differential light curve of J0925 in the R band.
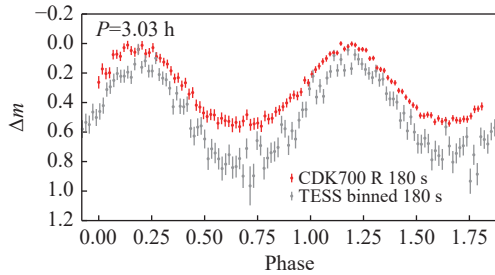

Fig. 8. Light curves of the candidate cataclysmic variable J0148.

0.155 836 day, and compare them with the ZTF g and r band data. The real orbital period is twice this period. However, because the time coverage of the data is less than a single orbital period and the levels of the primary and secondary minimums differ slightly, we chose to fold the data by half the orbital period. The phase profiles obtained from UCASST observations and ZTF are consistent.

7. DISCUSSION AND CONCLUSIONS

We have introduced UCASST and evaluated its photometric calibration, system performance, and basic site condition, finding that:
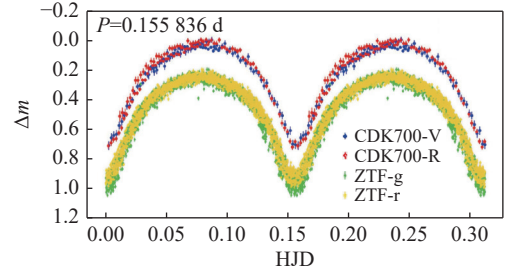
Fig. 9. Light curves of an EW-type eclipsing binary ATO J027+36.

(1) Considering the basic parameters of the Andor DZ936 CCD camera, bias, gain, and readout noise of the CCD demonstrated good stability over short and long periods of time. The CCD has a good linearity up to approximately 60 000 ADU and relatively low dark current for short exposure observations.

(2) Deriving the coefficients of photometric calibrations based on Landolt standard stars, including color terms, first-order atmospheric extinction coefficients, and photometric zero-points, we found that the color terms are relatively small. This indicated that the BVRI system for UCASST has similar respond curves to the standard system used by Landolt.

The atmospheric extinction coefficients presented are stable, and the atmospheric extinction coefficients are slightly larger than those measured at Xinglong Observatory, which indicates good atmospheric conditions. Additionally, the photometric zero-points are stable during observation nights during November and December of 2023, and dropped 1.7 in each band on May 30, 2024 (see Table 9). This can be rationalized as being because of newly constructed street lights illuminating the telescope system during observations (see Fig. 10). This also explains the drop of system throughput, the elevated sky background brightness, and the decline in limiting magnitudes (see Tables 10, 11, and 13).
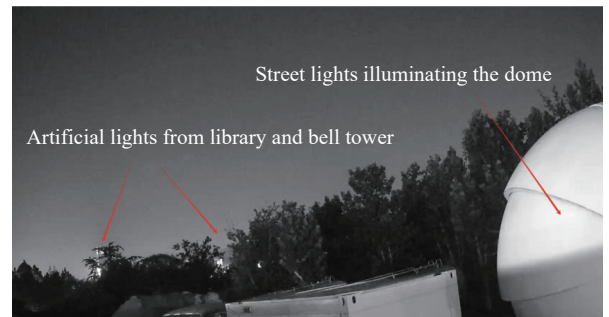

Fig. 10. Artificial lights illuminating the observation area.

(3) The system performance of UCASST is evaluated in this work, including system throughput, limiting magnitude, photometric precision, and sky background brightness. The limiting magnitudes for UCASST, with $R_{SN} = 10$ and a 30 s exposure time, are 16.5 in the B band, 16.5 in the V band, 16.4 in the R band, and 16.1 in the I band. The photometric precision for a 30 s exposure is ≤0.01 mag for stars brighter than 13.6 in the B

and V bands, 13.5 in the R band, and 13.0 in the I band. The sky background brightness at the observation site is much higher than that of other professional observatories and continues to increase.

Because UCASST is located on the Yan-qi Lake campus of UCAS, the effect of the artificial lights is severe, which directly leads to limited observation depth and low SNR of observations. We strongly urge that the effects of artificial light in the vicinity of UCASST should be minimized during observation time so that UCASST can be used under the best possible observation conditions.

UCASST can be used for limited scientific research, such as studying bright binaries, observing nearby supernovae, monitoring CVs, and observing bright occultations. It is also well-suited to teaching purposes.

ACKNOWLEDGMENTS

AUTHOR CONTRIBUTIONS

Yiming Mao conceived the ideas, implemented the study, and wrote the paper. Liang Ge and Hong Wu revised the paper. Yongkang Sun performed scientific analysis of the CVs. Jingxiao Luo, Lifu Zhang, and Minglin Wang participated in the early installation and testing of UCASST. Xunhao Chen and Renhao Ye performed the observations. E Xiang and Zhizhong Zhou provided ample technical support. All authors read and approved the final manuscript.

DECLARATION OF INTERESTS

The authors declare no competing interests.

REFERENCES

[1] Sicardy, B., Tej, A., Gomes-Júnior, A. R., et al. 2024. Constraints on the evolution of the Triton atmosphere from occultations: 1989–2022. *Astronomy & Astrophysics*, **682**: L24.

[2] Yuan, Y., Zhang, C., Li, F., et al. 2024. New constraints on Triton's atmosphere from the 6 October 2022 stellar occultation. *Astronomy & Astrophysics*, **684**: L13.

[3] Ohlson, D., Seth, A. C., Gallo, E., et al. 2024. The 50 Mpc Galaxy Catalog (50 MGC): Consistent and homogeneous masses, distances, colors, and morphologies. *The Astronomical Journal*, **167**(1): 31.

[4] Warner, B. 1995. Cataclysmic variable stars. Cambridge: Cambridge University Press.

[5] Warner, B. 2004. Rapid oscillations in cataclysmic variables. *Publications of Astronomical Society of the Pacific*, **116**(816): 115−132.

[6] Shappee, B. J., Prieto, J. L., Grupe, D., et al. 2014. The man behind the curtain: X-rays drive the UV through NIR variability in the 2013 active galactic nucleus outburst in NGC 2617. *The Astrophysical Journal*, **788**(1): 48.

[7] Bellm, E. C., Kulkarni, S. R., Graham, M. J., et al. 2019. The Zwicky Transient Facility: System overview, performance, and first results. *Publications of Astronomical Society of the Pacific*, **131**(995): 018002.

[8] Landolt, A. U. 1992. UBVRI photometric standard stars in the magnitude range 11.5<V<16.0 around the celestial equator. *The Astronomical Journal*, **104**: 340.

[9] Howell, S. B. 2000. Handbook of CCD Astronomy. Cambridge: Cambridge University Press.

[10] Huang, F., Li, J. Z., Wang, X. F., et al. 2012. The photometric system of the Tsinghua-NAOC 80-cm telescope at NAOC Xinglong Observatory. *Research in Astronomy and Astrophysics*, **12**(11): 1585−1596.

[11] Zhou, A. Y., Jiang, X. J., Zhang, Y. P., et al. 2009. MiCPhot: A prime-focus multicolor CCD photometer on the 85-cm Telescope. *Research in Astronomy and Astrophysics*, **9**(3): 349.

[12] Mu, H. Y., Fan, Z., Zhu, Y. N., et al. 2024. Astronomical test with CMOS on the 60 cm Telescope at the Xinglong Observatory, NAOC. *Research in Astronomy and Astrophysics*, **24**(5): 055009.

[13] Kinoshita, D., Chen, C. W., Lin, H. C., et al. 2005. Characteristics and performance of the CCD photometric system at Lulin Observatory. *Chinese Journal of Astronomy and Astrophysics*, **5**(3): 315−326.

[14] Shi, H. M., Qiao, Q. Y., Hu, J. Y., et al. 1998. Characterization of the CCD system at the BAO 60 cm reflector for photometry. *Acta Astrophysica Sinica*, **18**(1): 99−105. (in Chinese)

[15] Hu, S. M., Han, S. H., Guo, D. F., et al. 2014. The photometric system of the One-meter Telescope at Weihai Observatory of Shandong University. *Research in Astronomy and Astrophysics*, **14**(6): 719.

[16] Benn, C. R., Ellison, S. L. 1999. La Palma night-sky brightness. *arXiv: 9909153*.

[17] Patat, F. 2003. UBVRI night sky brightness during sunspot maximum at ESO-Paranal. *Astronomy & Astrophysics*, **400**(3): 1183−1198.

[18] Hou, W., Luo, A. L., Li, Y. B. et al. 2020. Spectroscopically identified cataclysmic variables from the LAMOST survey I. The sample. *The Astronomical Journal*, **159**(2): 43.

[19] Sun, Y. K., Cheng, Z. H., Ye, S., et al. 2021. A Catalog of 323 cataclysmic variables from LAMOST DR6. *The Astrophysical Journal, Supplement Series*, **257**(2): 65.